Chemical Engineering Journal 352 (2018) 1014–1021

Contents lists available at ScienceDirect

Chemical Engineering Journal

journal homepage: www.elsevier.com/locate/cej

Interplay among ozone and nitrogen oxides in air plasmas: Rapid change in plasma chemistry

Sanghoo Park[a], Wonho Choe[a,b,*], Cheorun Jo[c]

[a] Department of Nuclear and Quantum Engineering, Korea Advanced Institute of Science and Technology, 291 Daehak-ro, Yuseong-gu, Daejeon 34141, Republic of Korea
[b] Department of Physics, Korea Advanced Institute of Science and Technology, 291 Daehak-ro, Yuseong-gu, Daejeon 34141, Republic of Korea
[c] Department of Agricultural Biotechnology, Center for Food and Bioconvergence, and Research Institute of Agriculture and Life Science, Seoul National University, Seoul 08826, Republic of Korea

HIGHLIGHTS

- Experimental observation of an interplay among O_3 and nitrogen oxides in air plasma.
- Rapid transition of the plasma-chemistry mode (O_3-to-NO_2 dominant mode transition).
- Discussion in terms of chemical reaction set using zero-dimensional modelling.
- Effect of gas temperature on chemical characteristics of air plasmas.

GRAPHICAL ABSTRACT

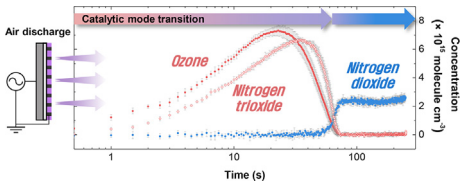

ARTICLE INFO

Keywords:
Air discharge
Plasma chemistry
Dielectric barrier discharge
Chemical interplay
Ozone
Nitrogen oxides
Gas temperature

ABSTRACT

Air is obligatorily used as a supply gas in most of the plasma-aided processing (*e.g.*, plasma-catalysis) systems because it is the most cost-effective approach, but the simultaneous production of gaseous ozone and nitrogen oxides is an unavoidable issue. Consequently, facilitating the separate production of ozone and nitrogen oxides is the primary requirement for achieving the desired plasma performance for specific purposes, yet it is poorly studied. Here, we report the chemical interplay among ozone and nitrogen oxides (*i.e.*, NO, NO_2, NO_3, N_2O_4, N_2O_5) in air-based plasmas using surface dielectric barrier discharge (DBD) actuators as a reference plasma. A gas-tight chamber containing a DBD apparatus was designed for in-situ optical absorption spectroscopy to measure the concentrations of the chemicals. The temporal evolution of each chemical was successfully observed, and a rapid change in the plasma-chemistry mode (*i.e.*, O_3- to NO_2-dominant mode) was clearly demonstrated. As a control parameter, the gas temperature, which ranged from 25 °C to 250 °C, was set in separate experiments. As the gas temperature was increased, ozone decomposed faster, while NO_2 became a dominant chemical species in the reactor earlier. All experimental results were compared with zero-dimensional modeling results, and the interplay among ozone and nitrogen oxides in air plasma was qualitatively analyzed. The gas temperature, which can be influenced by ohmic heating of the plasma itself, convective cooling from external or internal gas flow, or external settings, should be carefully considered for future study and commercialization.

* Corresponding author at: Department of Nuclear and Quantum Engineering, Korea Advanced Institute of Science and Technology, 291 Daehak-ro, Yuseong-gu, Daejeon 34141, Republic of Korea.
E-mail address: wchoe@kaist.ac.kr (W. Choe).

https://doi.org/10.1016/j.cej.2018.07.039
Received 23 February 2018; Received in revised form 12 June 2018; Accepted 4 July 2018
Available online 05 July 2018
1385-8947/

1. Introduction

In recent years, as the concept of decentralized chemical manufacturing is gradually gaining acceptance in chemical and relevant industries for practical applications, demands for compact and easy-to-use facilities (to replace full-scale plants) with high overall efficiencies have opened a new era of plasma chemistry research and expanded related research areas. One good example is that electricity-driven plasma processes, which were well established and used for nitrogen fixation before the Haber-Bosch technique was developed, are now considered again to be very attractive candidates among several alternatives for replacing the Haber-Bosch technique [1,2]. The highest NO_x concentration of 5700 ppm was obtained in a plasma reactor with γ-Al_2O_3 catalyst, and a series of 5% WO_3/γ-Al_2O_3 catalysts further increased the NO_x concentration by approximately 10% [2]. Likewise, active attempts to employ plasma technology for a wide range of applications have shown impressive results, and plasma is sometimes combined with catalyst because it promises dramatic improvements in the catalytic or energy efficiency over that of a plasma or catalyst alone [3]. The presence of plasma in the catalytic process enhances the chemical reactivity by increasing the chemical production of reactive species via electron-impact reactions, which is thermodynamically unfavorable via chemical reactions at low gas temperatures. In addition, it is well known that the plasma improves the surface characteristics of catalysts [4,5], emits photons for photocatalytic processes [6], and acts as oxidative media [7].

Most recently, a special attention has been paid to utilization of low-temperature plasmas as chemical agents, whose action is related to reactive oxygen and nitrogen species, for food and agricultural applications [8–10]. Yong et al. reported that a flexible thin-layer plasma system effectively inactivate bacteria and mold on beef jerky in a commercial package [11]. Jung et al. suggested that plasma-treated water (PTW) can be used instead of sodium nitrite ($NaNO_2$) as a nitrite source in curing meat products, and the sensory properties of food treated with PTW is the same as that of $NaNO_2$-treated food [12]. The approaches on decontamination of seeds against harmful fungi [13], enhancement of seed germination rate, yield, and plant growth [14,15], remediation of soil and water [16], and improvement of functional activities in biomaterials [17] using the plasma have confirmed the usefulness of the plasma technology in various fields of food and agriculture industry. Moreover, some research groups are now trying to commercialize bench-scale plasma systems for such plasma applications.

In most of the plasma-aided processing systems (including the plasma-catalysis) used for the applications introduced above, air is commonly or obligatorily used as a supply gas instead of pure nitrogen, oxygen, or synthetic air because compressing the ambient air using conventional compressors is the most cost-effective approach to improve operation and maintenance. In this case, the simultaneous production of gaseous ozone and nitrogen oxides is an unavoidable issue; thus, facilitating the separate production of ozone and nitrogen oxides is the main requirement for achieving the desired plasma performance for specific purposes. For example, in the case of nitrogen fixation via wet scrubbing or wet surface treatment, dinitrogen tetroxide (N_2O_4) and dinitrogen pentoxide (N_2O_5), formed by the deep oxidation of nitric oxide (NO) by abundant ozone (O_3) or other oxidizing agents, are favorable because the solubility of nitrogen oxides in water-based solutions increases with the valance state [18]. In contrast, ozone-free nitric oxide production is preferred for applications ranging from wound disinfection/healing to inhalation therapy [19]. However, the chemical reactions occurring in the plasma produced at atmospheric pressure are difficult to control, and the selectivity towards the desired products is rarely optimal. In this regard, there have been ongoing efforts to clarifying the chemical characteristics of air-based plasma. Shimizu et al. demonstrated the mode transition in ozone production in the surface air discharge and a correlation between time-averaged ozone concentration and the inactivation rate of *Escherichia coli* on adjacent agar plates [20]. Malik et al. reported that steady-state concentrations of O_3, NO, and NO_2 in the air-flowing plasma reactor, and these quantities were monitored remotely by sampling gas into commercial O_3 and NO_x analyzers [19].

Due to their attractive features, such as great operational reliability and reproducibility, atmospheric pressure dielectric barrier discharge (DBD) actuators have become one of the most scientifically interesting and practically useful discharges not only for ozone production but also for the entirety of low-temperature plasma chemistry. As a bold attempt to address the above issues, we employed a DBD apparatus as a reference air-based plasma source. Here we report the chemical interplay among ozone and nitrogen oxides over a gas temperature range of 25–250 °C in an air DBD system, and a rapid change in plasma-chemistry modes associated with ozone and nitrogen oxides is demonstrated. Considering practical application aspect of plasmas, the range of gas temperature is wide from room temperature to hundreds of Celsius, whereas the fixed input power or voltage is usually employed in industrial plasma devices. Continuous changes in chemical composition during the DBD operation were observed using an in-situ optical absorption spectroscopy with a 0.5-s time resolution. In the early discharge phase, an O_3-dominant environment was created, but after a certain time, the transition to an NO_2-dominant mode occurred because O_3 is rapidly quenched. As the gas temperature was raised, this mode transition occurred earlier. To assess the experimental data in terms of chemical reactions, zero-dimensional numerical modeling was carried out. This will be the first experimental demonstration and clear report about the simultaneous evolution of O_3 and nitrogen oxides.

2. Experimental

2.1. DBD apparatus and relevant diagnostic system

Fig. 1(a) shows the top and side views of the plasma reactor, which consisted of a gas-tight chamber with a DBD apparatus and the relevant experimental setup. The gas-tight chamber was made of stainless-steel and had two fused silica windows for UV–visible absorption spectroscopy. The DBD source consisted of two sheet electrodes covering each side of a 1-mm-thick, $100 \times 100\,mm^2$ fused silica plate. One electrode was connected to a neon transformer (NT Electronics NTO-1501). Considering the practical aspects of the power supply, a conventional neon transformer was used instead of a cutting-edge, high-cost power supply. The electric characteristics of the neon transformer are provided in Fig. S1 (in Supporting Information). The input voltage for the neon transformer was controlled using a voltage variable transformer (HC Transformer HCS-2SD10) and was set at AC 120 V. The ground electrode in direct contact with the discharge was composed of a nickel–chromium alloy to prevent rapid oxidation of the electrode because of the presence of highly oxidizing species during plasma operation. Air surface discharge was generated at the open surface of the ground electrode with 49 patterns of $7 \times 7\,mm^2$ rounded squares, as seen in Fig. S2, in dry synthetic air without any gas supply. To obtain charge–voltage (Q–V) Lissajous curves for measuring the dissipated power by plasma (see Fig. S3), a 100-nF blocking capacitor was serially connected to the ground electrode, as depicted in Fig. 1(a). The voltage applied to the DBD source was measured using a 1000:1 high-voltage probe (Tektronix P6015A), while the voltage across the 100-nF capacitor was measured using a 10:1 voltage probe (Tektronix P2100). A hot plate (DAIHAN Scientific MSH-20D) was used to control the temperature of the plasma reactor. Fig. 1(b) presents the time-averaged dissipated power by the plasma at different gas temperatures.

2.2. In-situ ozone and nitrogen oxide measurements

To determine the absolute concentration of chemical species, absorption spectra over the wavelength (λ) range of 200–800 nm were

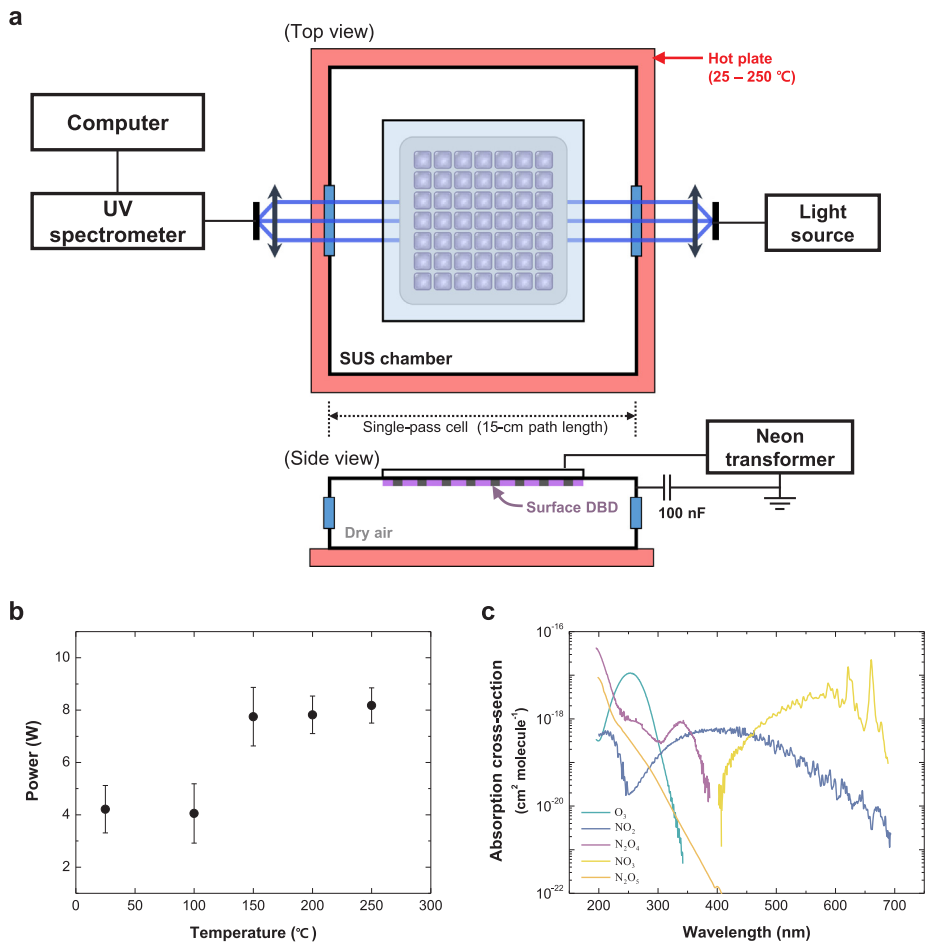

Fig. 1. (a) Schematic of a plasma chamber and the relevant experimental setup for producing a surface air DBD and for the in-situ monitoring of ozone and nitrogen oxides at 760 Torr in a gas temperature range of 25–250 °C. (b) Dissipated power by plasma obtained from a *Q–V* Lissajous curve. (c) Absorption cross-section of each chemical species in a wavelength range of 200–700 nm; O_3 [21], NO_2 [22], NO_3 [23], N_2O_4 [24], N_2O_5 [25]. The error bars in (c) indicate the standard deviation of the dissipated power during plasma operation.

obtained using the combination of a halogen-deuterium lamp (Ocean Optics ISS-UV/VIS) and a spectrometer (Ocean Optics Maya2000 Pro). The absorption path length was set at 150 mm. The UV–visible light was transferred through an optical fiber (Ocean Optics QP400-2-SR), with a core diameter of 400 μm, and the fiber was connected to a collimating lens adapter (Ocean Optics 74-UV) to collimate the light into the chamber. The same optical configuration was used to detect the light passing through the chamber by the spectrometer, as illustrated in Fig. 1(a). An integration time of 100 ms was used, and every spectrum used for a concentration measurement was obtained by averaging five 100 ms-integrated spectra; the time interval between adjacent spectra was 500 ms. This time resolution of the measurements was sufficient for measuring ozone and nitrogen oxides, which are long-lived chemical species (a lifetime $\tau \gg 1$ s). All spectra were automatically recorded by a computer. Example reference and absorption spectra are provided in Fig. S4.

An absorption cross-section (σ) of ozone and nitrogen oxides over a spectral range of 200–700 nm is shown in Fig. 1(c). Each measurable species, except N_2O_4 and N_2O_5, have its relatively highest cross-section at different wavelengths: O_3 at 253 nm, nitrogen dioxide (NO_2) at 400 nm, and nitrogen trioxide (NO_3) at 660 nm. To obtain the synthetic absorption spectra or chemical concentrations, the absorbance $A(\lambda)$ was calculated following the Beer-Lambert law:

$$A(\lambda) = \sum_i n_i\, l\, \sigma_i(\lambda), \tag{1}$$

where n is the concentration of chemical species in molecule·cm^{-3}, l is the absorption path length in centimeters, and the subscript i indicates each chemical species.

Nitrous oxide (N_2O) is actively produced in such air discharges [26], however its concentration could not be experimentally determined by an in-situ optical absorption spectroscopy in our experiments. This is because the absorption cross section of N_2O is relatively much lower than that of other species and absorption spectrum of N_2O is largely overlapped with those of N_2O_4 and N_2O_5. The experimental information on NO is not provided by the same reason.

2.3. Experimental procedure

First, the reactor temperature was set at 25, 100, 150, 200, or 250 °C for each experiment using a hot plate. Before every experiment, the ambient air or air activated by plasma during the previous experiment was replaced by dry air (20.8% oxygen with balance nitrogen, 0% relative humidity). After dry air had filled the chamber, the surface DBD was produced, and then the concentrations of chemical species were measured using UV–visible absorption spectroscopy. Each experiment at a fixed gas temperature was repeated ten times. All experiments were performed with the same devices without any replacements. There was no aging effect on the DBD system during all experiments in this work.

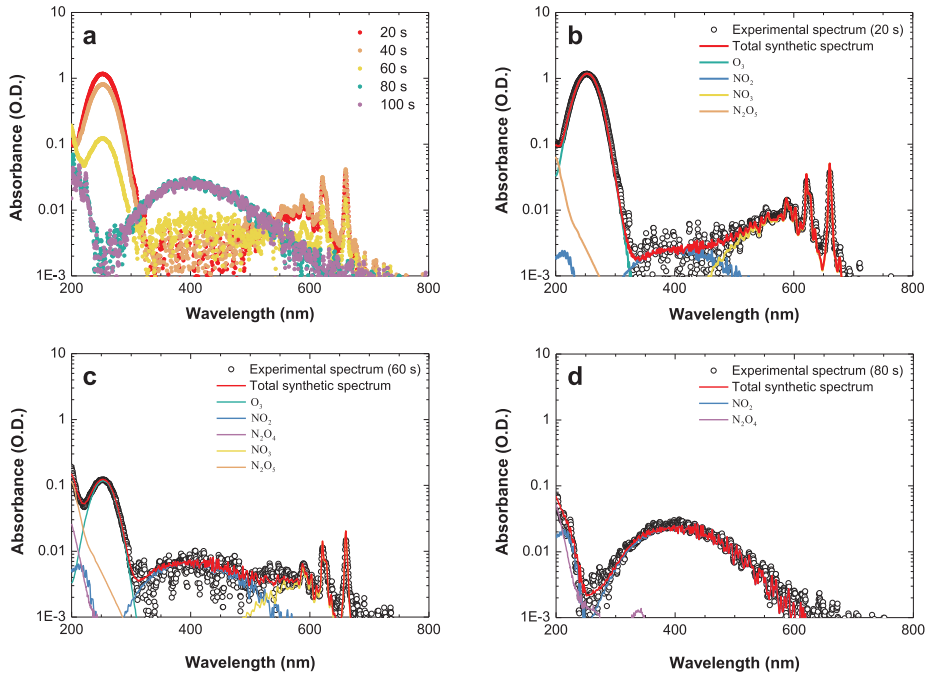

Fig. 2. (a) Absorption spectra over the discharge time. Each spectrum is presented in (b–d) with fitted synthetic curves obtained from the absorption cross-section of each chemical species. Plotting the absorbance on a logarithmic scale clearly separates the chemical species.

3. Results and discussion

3.1. Temporal dynamics of ozone and nitrogen oxides

The temporal dynamics and chemical interplay among O_3 and nitrogen oxides were investigated using in-situ optical absorption spectroscopy. The case of a gas temperature of 150 °C will be discussed as a representative example, and the absorption spectroscopy results are presented in Fig. 2. As shown in Fig. 2(a), the spectral distribution of absorbance from 200 to 800 nm changes dramatically over the discharge time (10–80 s) and is sufficient for identification of chemical species.

Fig. 2(b–d) shows the experimental absorption spectra and fitted synthetic spectra at different discharge times. In Fig. 2(b), the total synthetic spectrum denoted by a red solid line is a convolution of the spectrum of each species and yields 0.7×10^{16} molecule cm^{-3} of O_3, 3.0×10^{14} molecule cm^{-3} of NO_2, 1.5×10^{14} molecule cm^{-3} of NO_3, and 5.0×10^{14} molecule cm^{-3} of N_2O_5; these data fit well with the measured spectrum. As shown in Fig. 2(b), at the early discharge stage (20 s), strong peaks are found at 253 nm and 660 nm that are corresponding to O_3 and NO_3, respectively. This spectrum demonstrates that O_3 rapidly formed after the discharge was turned on, and the presence of abundant O_3 enables the high oxidation of NO, thereby resulting in the active production of NO_3 and N_2O_5. A measured absorption spectrum at 20 s and 60 s in the spectral range of 300–500 nm was spectrally contaminated by nitrogen molecular bands, $N_2(C^2\Pi_u-B^2\Pi_g)$ and $N_2^+(B^2\Sigma_u^+-X^2\Sigma_g^+)$, which were remotely formed from the long-lived molecules $N_2(A^3\Sigma_u^+)$ [27]. Nonetheless, the contribution of each chemical species in the measured absorption spectrum was clearly identified, and the composed synthetic spectrum was well fitted. Compared with the spectrum at 20 s, the fitted synthetic spectrum shows that the concentrations of O_3 and NO_3 decreased spontaneously at 60 s, whereas that of NO_2 at 400 nm increased noticeably by 2.67 times. A detailed discussion with a numerical modelling will be provided below. Fig. 2(d) shows the measured spectrum at steady state (> 80 s) with synthetic spectra of each chemical. It appears that numerous absorbance peaks in the 250–300 nm range would originate from the molecular band emission of $NO(A^2\Sigma^+-X^2\Pi)$. NO_2 and N_2O_4 became the two dominant absorbers, while the contributions of other chemicals present in the early discharge stage to the optical density was totally diminished. The fitting result of the absorption spectra used to obtain the absolute concentrations of chemical species are discussed below.

Shown in Fig. 3 is the temporal evolution of the chemical concentrations over the on-discharge time. Ozone was actively formed right after the plasma was turned on, and its concentration gradually increased, as seen in Fig. 3(a). However, at certain times, increasing trends were reversed. The formation time, defined as the time reaching the peak concentration, became shorter with increasing gas temperature. The curves show that the decay of O_3 was much faster than first-order decomposition, indicating that the O_3 decay was not solely caused by the thermal decomposition. In contrast to O_3, NO_2 was not noticeably produced right after the plasma was turned on, but rapid increases in its content were observed [see Fig. 3(b)]. After a rapid increase, the NO_2 concentration reached steady-state. The overall temporal trends of NO_3 were quite similar to those of O_3, as shown in Fig. 3(c). The maximum achievable concentration of all species over the discharge time decreased as the gas temperature was increased. The concentrations of all three species at 150 °C over the discharge time are replotted in Fig. 3(d) for comparison. The figure clearly demonstrates that the NO_2 concentration curve crosses over the O_3 and NO_3 concentration curves. Hereafter, this time is referred to as the transition time.

3.2. Chemical properties dependent on the gas temperature

To assess the reactivity of the plasma reactor, which is determined by the concentration of O_3 or NO_x, the maximum available concentration of O_3 and NO_2 and the aforementioned transition time are obtained at a given gas temperature, as seen in Fig. 4(a) and (b), respectively. The maximum O_3 concentration dramatically decreased by 25 times (from 3.81×10^{16} to 0.15×10^{16} molecule cm^{-3}) as the gas temperature was increased from 25 °C to 250 °C because the loss rate of O_3 increased. In addition, the maximum NO_2 concentration also decreased because oxygen atoms, which are a major source for NO_2 production, are consumed in the reaction $N_2 + O \rightarrow NO + N$. The transition time decreased almost exponentially with an increasing gas temperature. Therefore, NO and NO_2 can be the dominant species during operation.

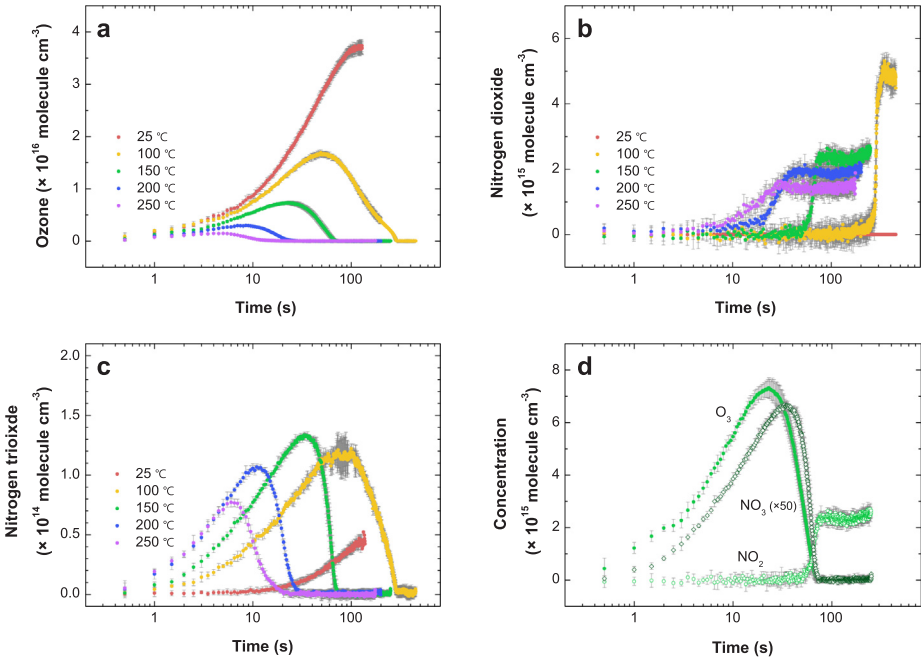

Fig. 3. Temporal evolution of the concentrations of (a) ozone, (b) nitrogen dioxide, and (c) nitrogen trioxide at gas temperatures of 25, 100, 150, 200, and 250 °C. The three concentrations at 150 °C are replotted in (d). The concentration of nitrogen trioxide in (d) is multiplied by 50 for comparison. All *x*-axes are on a logarithmic scale. Data are shown as the mean ± s.d. for all figures; the number of samples is 10.

At 250 °C, the mode transition rapidly occurred after 10 s, which was 27 times faster than that at 100 °C. According to Ref. [20], the discharge power density is a key parameter determining the transition behavior of O_3. However, the separate consideration of the effect of discharge power and gas temperature on such characteristics is nontrivial because, as is known, these two are related. It is worth noting that the discharge powers given in Fig. 1(b) are results of a constant input-voltage operation at different gas temperatures.

3.3. Zero-dimensional simulation for understanding the interplay among ozone and nitrogen oxides

A numerical simulation was dedicated to provide the qualitative analysis of experimental results in terms of chemical reaction. The temporal evolution of ozone and nitrogen oxides is described as a zero-dimensional chemical model in the plasma reactor; the model equations determine the time-dependent chemical concentrations in the reaction volume without diffusion. It is noteworthy that the reactor dimension is sufficiently smaller than the characteristic length scale of neutral reactions to approximate the interesting domain as a zero-dimensional problem [26]. In addition, as the flow field generated by plasma via electrohydrodynamic force makes the reactor well-convective [28,29], a zero-dimensional model is quite acceptable in this work. The surface DBD operated in dry air (20.8% oxygen with nitrogen balance) was considered the same as the experimental conditions. The initial concentrations of all the species, except air, atomic oxygen, and excited N_2 and O_2, were set at $10^4\,cm^{-3}$. The gas temperature was fixed at $T_g = 423$ K, corresponding to 150 °C.

The time-dependent continuity equation for all chemical species is as follows:

$$\frac{\partial n_i}{\partial t} = S_i - L_i, \tag{2}$$

where S_i and L_i, which are defined by $\sum_j k_j \prod n_{r,j}$, are the source and loss terms of n_i, respectively. k is the rate coefficient of chemical reactions, n_r is the concentration of the species involved in the reaction, and j indicates each chemical species involved in the reaction. The model takes into account 10 chemical species, including neutral oxygen and nitrogen atoms. In this study, the complete set of reactions is not necessary because other than these species in air-based plasma reactor are rarely produced and react with ozone and nitrogen oxides. Table 1 lists all 36 reactions, which are categorized into three groups: atomic oxygen chemistry, atomic nitrogen chemistry, and ozone and nitrogen oxide reactions. Notably, this reduced reaction set might not be valid under different conditions because of the highly nonlinear nature of plasma chemistry, but our model results show good agreement with our experimental measurements of ozone and nitrogen oxides.

The model equations were solved using MATLAB software [40], and an ordinary differential equation solver ('ode15s') was used to solve the continuity equations. The calculations took only approximately 1.6 s for

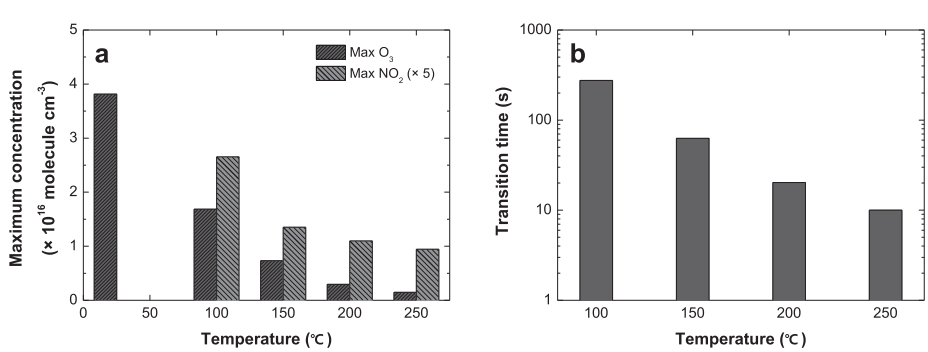

Fig. 4. (a) Maximum concentrations of ozone and nitrogen dioxide and (b) the transition time at different gas temperatures. The maximum concentrations of nitrogen dioxide are multiplied by 5 for the sake of comparison.

Table 1
Chemical reactions taking place inside the DBD reactor in dry air.

No.	Reaction	Rate coefficient	Reference
Atomic oxygen chemistry			
R1	$O + O + M \rightarrow O_2 + M$	$3.2 \times 10^{-47}\exp(900/T_g)$	[30]
R2	$O + O_2 + M \rightarrow O_3 + M$	$3.4 \times 10^{-46}(300/T_g)^{1.2}$	[30]
R3	$O + O_3 \rightarrow O_2 + O_2$	$8.0 \times 10^{-18}\exp(-2060/T_g)$	[30]
R4	$O + NO + M \rightarrow NO_2 + M$	$1.0 \times 10^{-43}(300/T_g)^{1.6}$	[30]
R5	$O + NO \rightarrow NO_2$	$3.01 \times 10^{-17}(T_g/298)^{0.3}$	[31]
R6	$O + NO_2 \rightarrow NO + O_2$	$5.5 \times 10^{-18}\exp(192/T_g)$	[32]
R7	$O + NO_2 + M \rightarrow NO_3 + M$	$1.31 \times 10^{-43}(298/T_g)^{1.5}$	[32]
R8	$O + NO_2 \rightarrow NO_3$	$2.3 \times 10^{-17}(T_g/298)^{0.2}$	[32]
R9	$O + NO_3 \rightarrow O_2 + NO_2$	1.7×10^{-17}	[30]
R10	$O + N_2(A^3\Sigma) \rightarrow NO + N(^2D)$	7.0×10^{-18}	[33]
R11	$O + N_2(v) \rightarrow NO + N$	1.0×10^{-17}	[33]
Atomic nitrogen chemistry			
R12	$N + N + M \rightarrow N_2 + M$	$8.3 \times 10^{-46}\exp(500/T_g)$	[33]
R13	$N + NO \rightarrow N_2 + O$	$2.1 \times 10^{-17}\exp(100/T_g)$	[30]
R14	$N + NO_2 \rightarrow N_2 O + O$	$5.8 \times 10^{-18}\exp(220/T_g)$	[30]
R15	$N + NO_2 \rightarrow N_2 + O + O$	9.1×10^{-19}	[34]
R16	$N + NO_2 + NO + NO$	6.0×10^{-19}	[34]
R17	$N + NO_2 + N_2 + O_2$	7.0×10^{-19}	[34]
R18	$N + O + M \rightarrow NO + M$	$6.3 \times 10^{-45}\exp(140/T_g)$	[30]
R19	$N + O_2 \rightarrow NO + O$	$4.47 \times 10^{-18}(T_g/298)\exp(-3270/T_g)$	[35]
R20	$N + O_3 \rightarrow NO + O_2$	5.0×10^{-22}	[34]
Ozone and nitrogen oxides reactions			
R21	$O_3 + NO \rightarrow NO_2 + O_2$	$1.8 \times 10^{-18}\exp(-1370/T_g)$	[30]
R22	$O_3 + NO_2 \rightarrow NO_3 + O_2$	$1.2 \times 10^{-19}\exp(-2450/T_g)$	[36]
R23	$O_3 + M \rightarrow O + O_2 + M$	$3.92 \times 10^{-16}\exp(-11400/T_g)$	[37]
R24	$O_3 + O_2(a^1\Delta) \rightarrow O + O_2 + O_2$	$5.2 \times 10^{-17}\exp(-2840/T_g)$	[30]
R25	$NO + NO_2 + M \rightarrow N_2O_3 + M$	$3.09 \times 10^{-46}(300/T_g)^{7.7}$	[31]
R26	$NO + NO_3 \rightarrow NO_2 + NO_2$	$1.8 \times 10^{-17}\exp(110/T_g)$	[30]
R27	$NO_2 + NO_2 + M \rightarrow N_2O_4 + M$	$1.44 \times 10^{-45}(298/T_g)^{3.8}$	[32]
R28	$NO_2 + NO_3 + M \rightarrow N_2O_5 + M$	$3.7 \times 10^{-42}(298/T_g)^{4.1}$	[32]
R29	$NO_2 + NO_3 \rightarrow NO_2 + NO + O_2$	$2.3 \times 10^{-19}\exp(-1600/T_g)$	[33]
R30	$NO_3 + NO_3 \rightarrow NO_2 + NO_2 + O_2$	$8.5 \times 10^{-19}\exp(-2450/T_g)$	[38]
R31	$N_2O_3 + M \rightarrow NO + NO_2 + M$	$1.09 \times 10^{-16}\exp(-2628/T_g)$	[32]
R32	$N_2O_4 + M \rightarrow NO_2 + NO_2 + M$	$1.11 \times 10^{-13}\exp(4952/T_g)$	[32]
R33	$N_2O_5 + M \rightarrow NO_2 + NO_3 + M$	$4.92 \times 10^{-11}\exp(-10040/T_g)$	[32]
R34	$N_2 O + N_2(A^3\Sigma) \rightarrow O + N_2 + N_2$	8.0×10^{-17}	[39]
R35	$N_2 O + N_2(A^3\Sigma) \rightarrow NO + N + N_2$	8.0×10^{-17}	[39]
R36	$NO_2 + N_2(A^3\Sigma) \rightarrow N_2 + NO + O$	1.3×10^{-17}	[30]

M denotes the third body, N_2 and O_2.
Units: Two-body reaction ($m^3\,s^{-1}$). Three-body reaction ($m^6\,s^{-1}$). Gas temperature T_g (K).

a 0.001–500 s period using a personal computer (a central processing unit with a 4-GHz processor base frequency and 16 GB of RAM). A widely accepted explanation for the rapid quenching of O_3 is that NO reacts with O_3 (reaction 21). In this model, the NO production in the reaction between vibrationally-excited nitrogen molecules [$N_2(v)$, where v is the vibrational quantum number] and O atoms is employed (reaction 11) [20]. To the best of our knowledge, other than reaction 11, the reactions still cannot explain the rapid increase in NO that results in the rapid quenching of O_3. The concentration of vibrationally-excited N_2, $n_{N_2(v)}$, and the vibrational temperature of N_2 molecules, T_v, were determined as follows [20]:

$$n_{N_2(v)} = n_{N_2} F_{v>12} = n_{N_2}\exp\left(-\frac{12\Delta\varepsilon_v}{k_b T_v}\right), \tag{3}$$

$$T_v = T_g + T_v^0[1-\exp(-t/\tau_v)], \tag{4}$$

where k_b is the Boltzmann constant, $\Delta\varepsilon_v$ (= 0.29 eV) is the vibrational energy for a harmonic oscillator, T_v^0 is the vibrational temperature at steady state, and τ_v is the time constant of the vibrational temperature increase.

The modeling results are discussed in the following. The comparison of the measured concentrations with the fitted model data is presented in Fig. 5(a). The gray scatter points represent the same experimental data set given in Fig. 3(d). The fitted parameters were $T_v^0 = 3100$ K, $\tau_v = 25$ s, $n_O = 6 \times 10^{11}\,cm^{-3}$, $n_{N_2(A)} = 1.5 \times 10^{11}\,cm^{-3}$, and $n_{O_2(a)} = 9.8 \times 10^{11}\,cm^{-3}$. The three concentrations were constant over the tested time period. 3100 K of T_v^0 was employed based on optical emission spectroscopy, as provided in Fig. S5. The fitted results show qualitatively good agreement with the experimental result, but a local discrepancy between the modeled and experimental results for the NO_2 concentration existed at 60–150 s. This discrepancy may have derived from the absence of charged-species reactions and a constant n_O over the discharge time in the model. Atomic oxygen concentration is temporally affected by charged particle reactions within one discharge period (*e.g.*, 0.1 ms, corresponding to 10 kHz) [26]. Thus, such rapid variation in neutral particle concentrations is hard to be described by

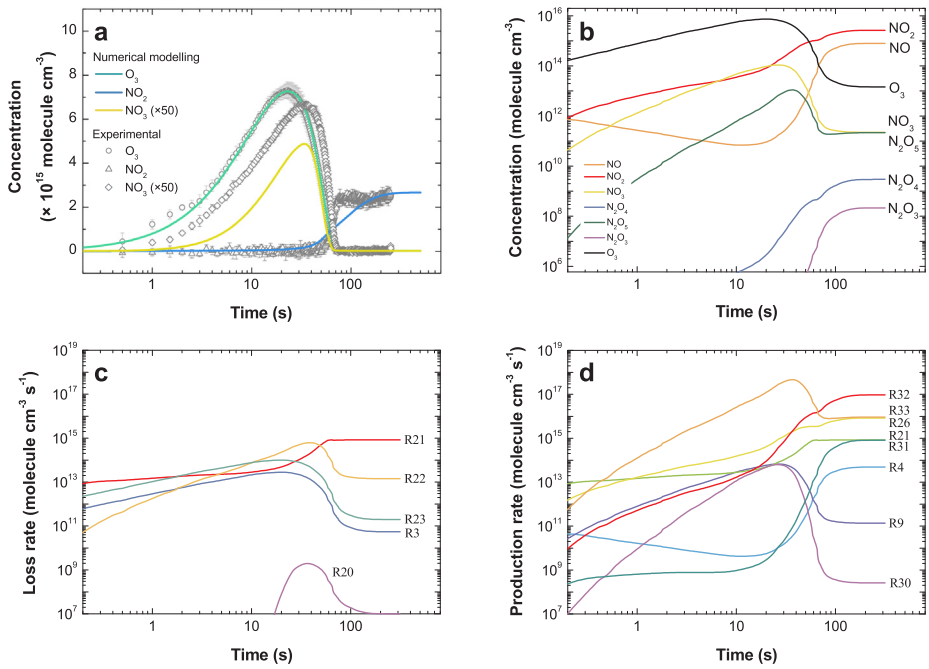

Fig. 5. Numerical modeling results: (a) temporal evolution of ozone and nitrogen oxides with the same curves in Fig. 3(d), (b) comparison of the chemical concentrations determined by the model at 150 °C, (c) time-dependent loss rate of ozone and (d) production rate of nitrogen dioxide via each chemical reaction.

our numerical model. Nevertheless, the concentrations at steady state are consistent. The modeling results for the NO_3 concentration (green line) were slightly lower than the experimental results (diamond scatter points), but both trends are identical. The maximum of the NO_3 concentration appeared later than that of O_3 because NO_3 was continuously produced via reactions 7 and 8 while O_3 decreased. The temporal evolution of the ozone and nitrogen oxides concentrations are presented in Fig. 5(b). Ozone was rapidly formed when the discharge was turned on via third-body reaction of O_2 and O, and its concentration increased above the order of 10^{14}–10^{15} cm^{-3}. Due partly to oxidation by ozone, the concentration of NO monotonically decreased, whereas those of NO_2 and NO_3 gradually increased. The increasing and decreasing trends of NO_3 and N_2O_5 were similar to the trend of O_3. At a certain time, the decreasing trend of NO concentration is reversed due primarily to reaction 11. This rapid increase in NO directly impacted the O_3 decomposition and NO_3 and N_2O_5 as well. In contrast, with increasing NO concentration, N_2O_4 and N_2O_3 increased, as seen in Fig. 5(b). This trend indicates that the formation of O_3 via reaction 1 and the extensive oxidation of NO by O_3 were prevented. In this regard, the chemical species can be divided into two groups: one consisting of O_3, NO_3, and N_2O_5 and the other consisting of NO, NO_2, N_2O_3, and N_2O_4. After the transition, all chemicals reached steady state; the concentrations of NO and NO_2 were 55 and 182 times higher, respectively, than that of O_3. Besides, the concentration of O_3 dropped dramatically from 7.48×10^{15} to 1.47×10^{13} cm^{-3}. Under this condition, NO_2 was more abundant than NO, but NO_2 could be suppressed by further reducing O_3 via thermal decomposition and other quenching reactions.

Fig. 5(c) and (d) show the loss rate of O_3 and the production rate of NO_2, respectively, via each chemical reaction given in Table 1. The curves depicted in Fig. 5(c) indicate four major loss channels for O_3, beginning with similar contributions. After the transition, O_3 was mainly quenched by NO via reaction 17. As interpreted previously, the rapid increase in NO prevented O_3 formation, resulting in significant limitations on the oxidation of nitrogen oxides. The production of NO_2 via reactions 16, 25, and 28 decreased after the transition due to a decrease in the NO_3 concentration.

4. Conclusion

The chemical characteristics of an air-based plasma system and its gas temperature dependence over the range of 25–250 °C were revealed in experiments with a surface DBD apparatus. In all cases, at the early stage of discharge, ozone formed rapidly and became the first major chemical in the plasma reactor. After the transition time inferred above, NO and NO_2 became the dominant species, whereas the level of O_3 was reasonably diminished. The maximum concentration of O_3 dramatically decreased by 25 times as the gas temperature increased from 25 to 250 °C, and that of NO_2 decreased as well. Notably, these decreases were not exclusively due to a decreased air number density with increasing gas temperature (according to the ideal gas law). The transition time exponentially decreased with increasing gas temperature. At 250 °C, the mode transition rapidly occurred after 10 s, which was 28 times faster than that at 100 °C. Based on our model results, we conclude that O_3 is mainly quenched by NO, of which the production rate is proportional to the N_2 vibrational temperature. Our findings clearly indicate that the gas temperature determines the chemical constituents present during early discharge and T_v, thereby playing a crucial role in the chemical characteristics of plasma systems in air. Consequently, the gas temperature, which can be influenced by ohmic heating of the surface discharge itself, convective cooling from the external gas flow, or external settings, should be considered for future study and commercialization. This study will be an informative and basic reference for plasma chemistry studies and further application of the plasma system in various fields of interest including food and agriculture industries.

Author contributions

All authors conceived of the experiments. S.P. conducted all experiments, and W.C. supervised the work. S.P. have prepared the manuscript and figures, and all authors have participated in the improvement of the paper.

Acknowledgement

The authors thank Youbong Lim and Plasmapp Ltd. Co. for technical

assistance. This work was supported by the R&D Program of 'Plasma Advanced Technology for Agriculture and Food (Plasma Farming)' through the National Fusion Research Institute of Korea (NFRI) funded by Korean government.

Appendix A. Supplementary data

Supplementary data associated with this article can be found, in the online version, at https://doi.org/10.1016/j.cej.2018.07.039.

References

[1] M. Iwamoto, M. Akiyama, K. Aihara, T. Deguchi, Ammonia synthesis on wool-like Au, Pt, Pd, Ag, or Cu electrode catalysts in nonthermal atmospheric-pressure plasma of N_2 and H_2, ACS Catal. 7 (2017) 6924–6929.
[2] B.S. Patil, N. Cherkasov, J. Lang, A.O. Ibhabon, V. Hessel, Q. Wang, Low temperature plasma-catalytic NO_x synthesis in a packed DBD reactor: effect of support materials and supported active metal oxides, Appl. Catal., B 194 (2016) 123–133.
[3] J.C. Whitehead, Plasma–catalysis: the known knowns, the known unknowns and the unknown unknowns, J. Phys. D: Appl. Phys. 49 (2016) 243001.
[4] G. Chen, N. Britun, T. Godfroid, V. Georgieva, R. Snyders, M.-P. Delplancke-Ogletree, An overview of CO_2 conversion in a microwave discharge: the role of plasma-catalysis, J. Phys. D: Appl. Phys. 50 (2017) 084001.
[5] J.C. Whitehead, Plasma catalysis: a solution for environmental problems, Pure Appl. Chem. 82 (2010) 1329–1336.
[6] E.C. Neyts, K. Ostrikov, M.K. Sunkara, A. Bogaerts, Plasma catalysis: synergistic effects at the nanoscale, Chem. Rev. 115 (2015) 13408–13446.
[7] H.T.Q. An, T.P. Huu, T.L. Van, J.M. Cormier, A. Khacef, Application of atmospheric non thermal plasma-catalysis hybrid system for air pollution control: toluene removal, Catal. Today 176 (2011) 474–477.
[8] N.N. Misra, C. Jo, Applications of cold plasma technology for microbiological safety in meat industry, Trends Food Sci. Technol. 64 (2017) 74–86.
[9] J.Y. Park, S. Park, W. Choe, H.I. Yong, C. Jo, K. Kim, Plasma-functionalized solution: a potent antimicrobial agent for biomedical applications from antibacterial therapeutics to biomaterial surface engineering, ACS Appl. Mater. Interfaces 9 (2017) 43470–43477.
[10] D.P. Park, K. Davis, S. Gilani, C.-A. Alonzo, D. Dobrynin, G. Friedman, A. Fridman, A. Rabinovich, G. Fridman, Reactive nitrogen species produced in water by non-equilibrium plasma increase plant growth rate and nutritional yield, Curr. Appl. Phys. 13 (2013) S19–S29.
[11] H.I. Yong, H. Lee, S. Park, J. Park, W. Choe, S. Jung, C. Jo, Flexible thin-layer plasma inactivation of bacteria and mold survival in beef jerky packaging and its effects on the meat's physicochemical properties, Meat Sci. 123 (2017) 151–156.
[12] S. Jung, H.J. Kim, S. Park, H.I. Yong, J.H. Choe, H.-J. Jeon, W. Choe, C. Jo, The use of atmospheric pressure plasma-treated water as a source of nitrite for emulsion-type sausage, Meat Sci. 108 (2015) 132–137.
[13] S. Iseki, T. Ohta, A. Aomatsu, M. Ito, H. Kano, Y. Higashijima, M. Hori, Rapid inactivation of Penicillium digitatum spores using high-density nonequilibrium atmospheric pressure plasma, Appl. Phys. Lett. 96 (2010) 153704.
[14] E. Bormashenko, R. Grynyov, Y. Bormashenki, E. Drori, Cold radiofrequency plasma treatment modifies wettability and germination speed of plant seeds, Sci. Rep. 2 (2012) 741.
[15] L. Ling, J. Jiafeng, L. Jiangang, S. Minchong, H. Xin, S. Hanliang, D. Yuanhua, Effects of cold plasma treatment on seed germination and seedling growth of soybean, Sci. Rep. 4 (2014) 5859.
[16] N. Lu, J. Lou, C.H. Wang, J. Li, Y. Wu, Evaluating the effects of silent discharge plasma on remediation of acid scarlet GR-contaminated soil, Water Air Soil Pollut. 225 (2014) 1991.
[17] T.H. Kim, J. Lee, H.-J. Kim, C. Jo, Plasma-induced degradation of quercetin associated with the enhancement of biological activities, J. Agric. Food Chem. 65 (2017) 6929–6935.
[18] F. Lin, Z. Wang, Q. Ma, Y. Yang, R. Whiddon, Y. Zhu, K. Cen, Catalytic deep oxidation of NO by ozone over MnO_x loaded spherical alumina catalyst, Appl. Catal., B 198 (2016) 100–111.
[19] M.A. Malik, C. Juang, R. Heller, J. Lane, D. Hughes, K.H. Schoenbach, Ozone-free nitric oxide production using an atmospheric pressure surface discharge – a way to minimize nitrogen dioxide co-production, Chem. Eng. J. 283 (2016) 631–638.
[20] T. Shimizu, Y. Sakiyama, D.B. Graves, J.L. Zimmermann, G.E. Morfill, The dynamics of ozone generation and mode transition in air surface micro-discharge plasma at atmospheric pressure, New J. Phys. 14 (2012) 103028.
[21] D. Daumont, J. Brion, J. Charbonnier, J. Malicet, Ozone UV spectroscopy I: absorption cross-sections at room temperature, J. Atmos. Chem. 15 (1992) 145–155.
[22] W. Schneider, G.K. Moortgat, J.P. Burrows, G.S.J. Tyndall, Photochem. Photobiol. A 40 (1987) 195–217.
[23] S.P.J. Sander, Temperature dependence of the nitrogen trioxide absorption spectrum, Phys. Chem. 90 (1986) 4135–4142.
[24] A.M. Bass, A.E. Ledford, A.H.J. Laufer, Extinction coefficients of NO_2 and N_2O_4, Res. Natl. Bur. Stand. 80A (1976) 143–166.
[25] S.P. Sander, J. Abbatt, J.R. Barker, J.B. Burkholder, R.R. Friedl, D.M. Golden, R.E. Huie, C.E. Kolb, M.J. Kurylo, G.K. Moortgat, V.L. Orkin, P.H. Wine, Chemical Kinetics and Photochemical Data for Use in Atmospheric Studies, Evaluation Number 17, JPL Publication 10-6 Jet Propulsion Laboratory, Pasadena, 2011.
[26] Y. Sakiyama, D.B. Graves, H.-W. Chang, T. Shimizu, G.E. Morfill, Plasma chemistry model of surface microdischarge in humid air and dynamics of reactive neutral species, J. Phys. D: Appl. Phys. 45 (2012) 425201.
[27] P.A. Sá, V. Guerra, J. Loureiro, N. Sadeghi, Self-consistent kinetic model of the short-lived afterglow in flowing nitrogen, J. Phys. D: Appl. Phys. 37 (2004) 221–231.
[28] S. Park, U. Cvelbar, W. Choe, S.Y. Moon, The creation of electric wind due to the electrohydrodynamic force, Nat. Commun. 9 (2018) 371.
[29] G. Neretti, P. Seri, M. Taglioli, A. Shaw, F. Iza, C.A. Borghi, Geometry optimization of linear and annular plasma synthetic jet actuators, J. Phys. D: Appl. Phys. 50 (2017) 015201.
[30] J.T. Herron, D.S. Green, Chemical kinetics database and predictive schemes for nonthermal humid air plasma chemistry. Part II. Neutral species reactions, Plasma Chem. Plasma Process. 21 (2001) 459.
[31] M. Capitelli, C.M. Ferreira, B.F. Gordiets, A.I. Osipov, Plasma Kinetics in Atmospheric Gases, Splinger, Berlin, 2000.
[32] R. Atkinson, D.L. Baulch, R.A. Cox, J.N. Crowley, R.F. Hampson, R.G. Hynes, M.E. Jenkin, M.J. Rossi, J. Troe, Evaluated kinetic and photochemical data for atmospheric chemistry: Volume I – gas phase reactions of O_x, HO_x, NO_x and SO_x species, Atmos. Chem. Phys. 4 (2004) 1461–1738.
[33] R. Atkinson, D.L. Baulch, R.A. Cox, R.F. Hampson, J.A. Kerr, M.J. Rossi, J. Troe, J. Phys. Chem. Ref. Data 26 (1997) 1329–1499.
[34] O. Eichwald, M. Yousfi, A. Hennad, M.D. Benabdessadok, Coupling of chemical kinetics, gas dynamics, and charged particle kinetics models for the analysis of NO reduction from flue gases, J. Appl. Phys. 82 (1997) 4781.
[35] D.L. Baulch, C.J. Cobos, R.A. Cox, P. Frank, G. Hayman, Th. Just, J.A. Kerr, T. Murrells, M.J. Pilling, J. Troe, R.W. Walker, J. Warnatz, Evaluated kinetic data for combustion modelling supplement I, J. Phys. Chem. Ref. Data 23 (1994) 847–1033.
[36] R. Atkinson, D.L. Baulch, R.A. Cox, R.F. Hampson, J.A. Kerr, J. Troe, Evaluated kinetic and photochemical data for atmospheric chemistry: supplement IV, J. Phys. Chem. Ref. Data 21 (1992) 1125–1568.
[37] J.Y. Jeong, J. Park, I. Henins, S.E. Babayan, V.J. Tu, G.S. Selwyn, G. Ding, R.F. Hicks, Reaction chemistry in the afterglow of an oxygen – helium, atmospheric-pressure plasma, J. Phys. Chem. A 104 (2000) 8027–8032.
[38] H.S. Johnston, C.A. Cantrell, J.G. Calvert, Unimolecular decomposition of NO_3 to form NO and O_2 and a review of N_2O_5/NO_3 kinetics, J. Geophys. Res. 91 (1986) 5159–5172.
[39] H. Matzing, Chemical kinetics of flue gas cleaning by irradiation with electrons, Adv. Chem. Phys. 80 (2007) 315–402.
[40] MATLAB R2016a, The MathWorks, Natick, 2016.